Bulletin of the Seismological Society of America, Vol. 106, No. 2, pp. 785–798, April 2016, doi: 10.1785/0120150144

Application of UAV Photography to Refining the Slip Rate on the Pyramid Lake Fault Zone, Nevada

by Stephen Angster, Steven Wesnousky, Wei-liang Huang,* Graham Kent, Takashi Nakata, and Hideaki Goto

Abstract The Pyramid Lake fault zone (PLFZ) is a 50-km-long, active northwest-trending right-lateral fault in the northern Walker Lane, located ~30 km east of Reno, Nevada. Previous paleoearthquake and slip-rate studies report that the Pyramid Lake fault has produced four surface-rupturing paleoearthquakes since 15,475 ± 720 cal B.P., three of which occurred after 8980 ± 260 cal B.P., and has had an average minimum slip rate of 2.6 ± 0.3 mm/yr since the late Pleistocene. These observations imply that coseismic offset for each paleoearthquake averaged 7–9 m, larger than expected from empirical scaling relationships for a strike-slip fault of its length. To reconcile this discrepancy, we used a small camera-mounted unmanned aerial vehicle to develop high-resolution digital elevation models and interpret previously unreported right-laterally offset geomorphic features along the northern section of the PLFZ. Offset measurements at seven sites range from 8 to 21 m. The ages of displaced features are interpreted from previous lake level and mapping studies of Lake Lahontan. From these observations, slip-rate estimates at the sites range between 0.5 and 1.6 mm/yr. These lower values of slip rate require that coseismic displacements associated with previously reported paleoearthquakes average only 3–5 m, within the range that would be predicted from empirical scaling relationships of rupture length and coseismic displacement.

Introduction

High-density geospatial point datasets provide opportunities to observe, measure, and document geologic surface processes at higher resolution than alternative approaches, particularly in subtle or obscured landscapes that pose interpretive challenges in the field (Arrowsmith and Zielke, 2009; Gold *et al.*, 2013; Johnson *et al.*, 2014; Zielke *et al.*, 2015). The recent and rapid advancement in acquisition techniques provides quick, accurate, and very cost-effective methods for scientists to utilize high-resolution digital elevation data for geologic analysis (Bemis *et al.*, 2014; Johnson *et al.*, 2014). These advances provide the opportunity to reevaluate prior studies in which inconsistencies or controversies persist.

The Pyramid Lake fault zone (PLFZ) is a 50-km-long, active northwest-trending right-lateral fault in the northern Walker Lane (Fig. 1). Previous paleoearthquake and slip-rate studies indicate that the Pyramid Lake fault has produced four surface-rupturing paleoearthquakes since 15,475 ± 720 yr B.P., three of which occurred after 8980 ± 260 yr B.P., and has had an average minimum slip rate of 2.6 ± 0.3 mm/yr since the late Pleistocene (Anderson and Hawkins, 1984; Briggs and Wesnousky, 2004). Reconciling these observations with expected per-event displacements for a fault of its length is challenging. Specifically, coseismic offsets of 7–9 m during the latest three paleoearthquakes are required to satisfy the fault-slip rate, which is significantly larger than would generally be expected from empirical scaling relationships for a strike-slip fault of its 50 km length (Wells and Coppersmith, 1994; Wesnousky, 2008).

In this article, we present new observations of tectonically displaced geomorphic features along the PLFZ acquired from high-resolution (< 20 cm) digital elevation models (DEMs) developed from structure-from-motion (SFM) processing of aerial photography obtained from a multirotor unmanned aerial vehicle (UAV). The observations suggest a lower slip rate for the PLFZ and help resolve inconsistencies between per-event displacements predicted from previous slip-rate estimates and potential rupture length of the PLFZ.

Geologic Framework

Pyramid Lake Fault Zone Surface Trace and Offset Potential

The PLFZ is expressed as a relatively narrow (< 2.5 km wide) fault zone that continues for ~45 km from Fernley, Nevada, to the southern edge of Pyramid Lake as a northwest-trending right-lateral strike-slip fault (Fig. 2). Recent marine shallow seismic reflection interpretations of Eisses *et al.* (2015) show west-dipping strata focused at the southern end of Pyramid

*Now at College of Geologic Engineering and Surveying of Chang'an University, 126 Yanta Avenue, Yanta District, Xi'an, Shan'xi Province, China.

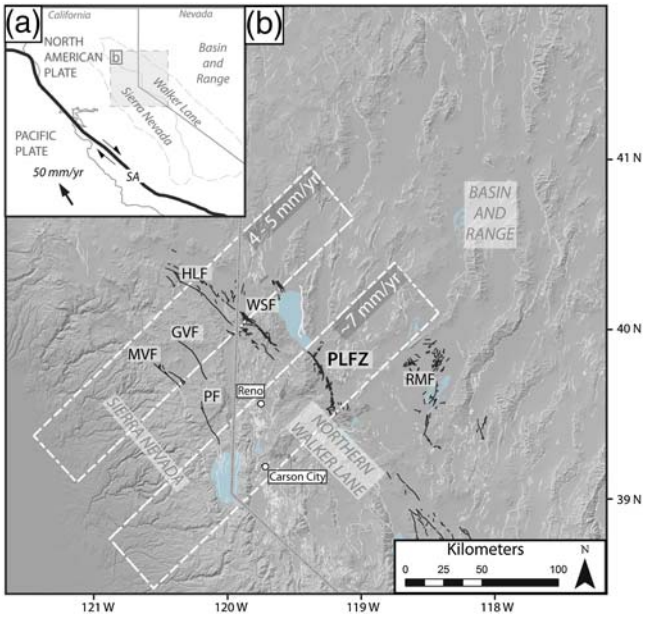

Figure 1. Regional hillshade and fault map of study area. Northwest-trending right-lateral strike-slip faults accommodating Walker Lane right-lateral shear are shown as solid black lines (PLFZ, Pyramid Lake fault Zone; PF, Polaris fault, MVF, Mohawk Valley fault; GVF, Grizzly Valley fault; HLF, Honey Lake fault; WSF, Warm Springs fault; RMF, Rainbow Mountain fault). Normal faults are shown in light gray. All faults modified from the U.S. Geological Survey Quaternary Fault and Fold Database (2006; see Data and Resources). White dashed boxes show geodetic transects from Bormann (2013) used to constrain strain rates for the northern Walker Lane. (Inset) Regional tectonic setting of the study area and its relation to the San Andreas (SA) fault system. The color version of this figure is available only in the electronic edition.

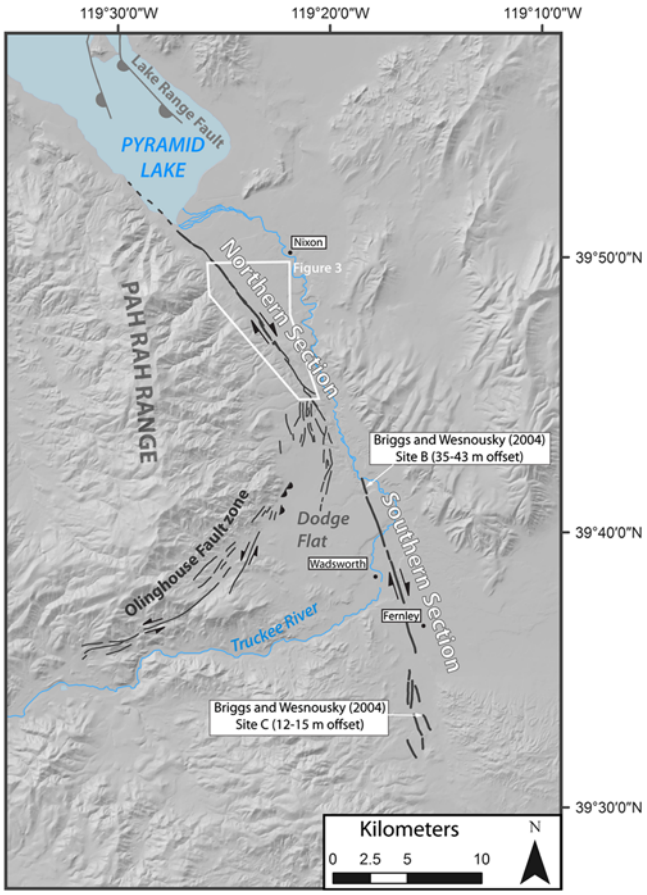

Figure 2. Map of PLFZ trace. Quaternary-active surface traces of the PLFZ are shown as a thick black solid line, and concealed traces (i.e., continued along elevation contour of associated extent) are shown as a dashed. The normal Lake Range fault and left-lateral Olinghouse fault are shown as thin black lines. Half circles on fault lines show down dropped sides of normal faults. The location of the Briggs and Wesnousky (2004) study sites referred to in the text is labeled and shown in detail in Figure 3. The color version of this figure is available only in the electronic edition.

Lake, suggesting that the PLFZ may extend for another 5 km as an east-dipping oblique fault along the west shore of the lake, which is characterized with more vertical displacement than to the south. This extends the length of the PLFZ to ~50 km. Further north, the character of regional faulting changes to north-northwest-trending normal faults (Fig. 1) and is dominantly expressed by the Lake Range fault, which bounds the east side of the lake and dips to the west (Figs. 1 and 2).

The emergent portion of the PLFZ has previously been divided into two sections based on geomorphic and structural observations (Bell and Slemmons, 1979; Anderson and Hawkins, 1984; Briggs and Wesnousky, 2004; Bell *et al.*, 2005). The southern section of the PLFZ begins south of Fernley, Nevada, and crosses Dodge Flat to where it parallels and is obscured by the steep bank of the Truckee River (Fig. 2). The southern section of the fault zone is expressed as multiple, aligned, discontinuous linear traces manifested as vegetation lineaments, scarps, and linear depressions within the middle of the valley. The northern limit of the southern section corresponds with the occurrence of distributed faulting and local extensional features near the intersection with the conjugate left-lateral Olinghouse fault (Sanders and Slemmons, 1996; Briggs and Wesnousky, 2005; Fig. 2).

The PLFZ is best defined in the northern section and displays a nearly continuous linear fault trace manifested as vegetation lineaments, uphill-facing scarps, bedrock and alluvial ridges, elongate depressions, and springs (Figs. 2 and 3). We targeted this portion of the fault because it crosses numerous gullies, drainage channels, and ridges, providing higher potential for preservation of displaced geomorphic features.

Geomorphic Units and Geochronologic Constraints

The PLFZ sits within the Pyramid Lake basin, which was once part of Lake Lahontan, a pluvial lake that reached its maximum highstand (Sehoo highstand) of ~1338 m at 15,475 ± 720 yr B.P. (15.5 ka) before rapidly desiccating to modern-day Pyramid Lake level (Benson and Thompson, 1987; Adams *et al.*, 1999; Briggs *et al.*, 2005). Remnant shoreline features, such as shoreline scarps, spits, tufa deposits, and modified fan surfaces, are prevalent within the Pyramid Lake basin and provide excellent late Pleistocene and

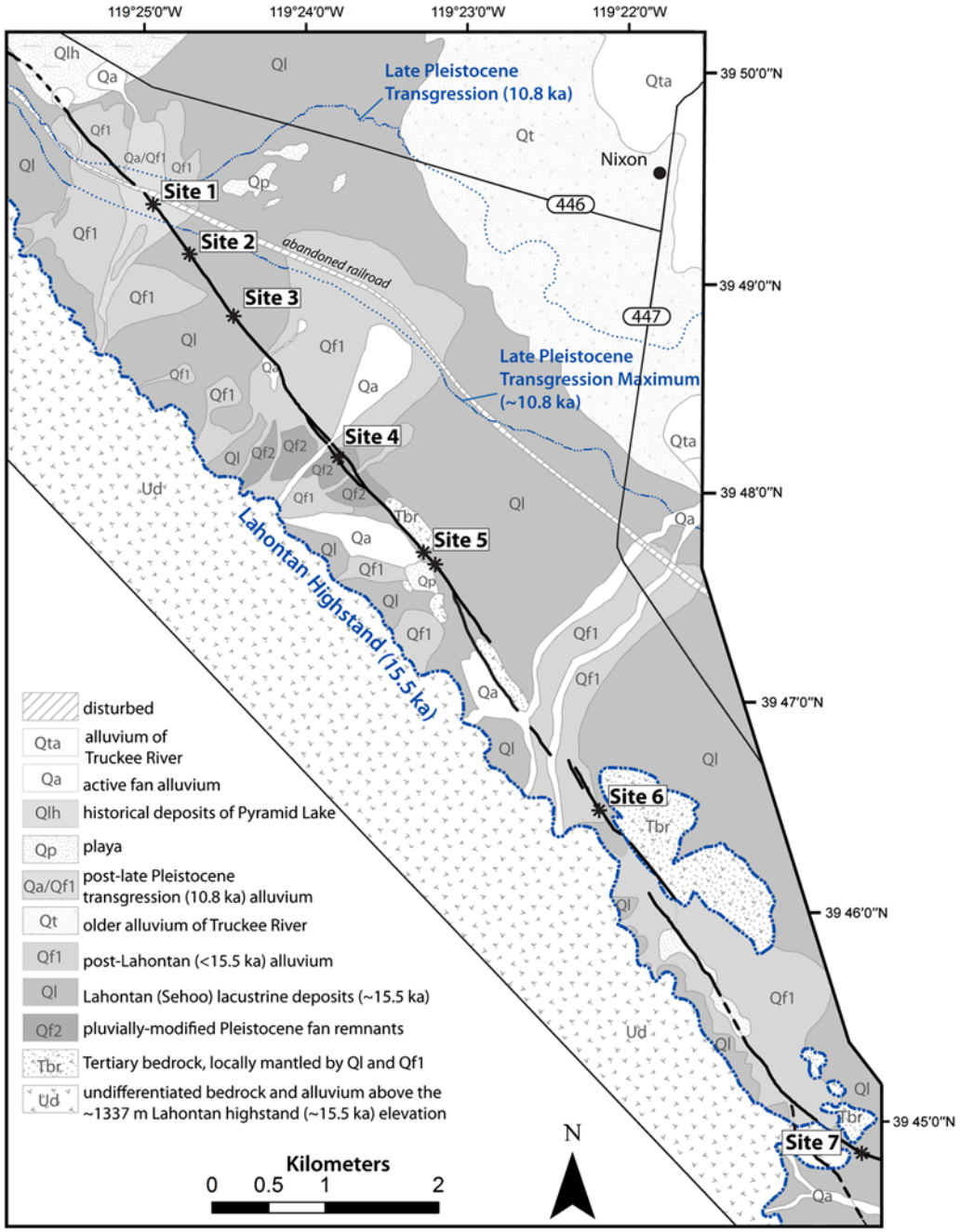

Figure 3. Surficial geologic map along the northern section of the PLFZ (modified from Briggs and Wesnousky, 2004). The fault trace is shown as a thick black line, and concealed traces are shown as a dashed line. Study sites 1–7 (asterisks) are shown along PLFZ. The contour of the Lahontan Sehoo highstand (15.5 ka) is shown by the thick dashed-dotted line. Contours of the late Pleistocene transgressions are shown with dashed-dotted lines, and concealed traces (i.e., continued along elevation contour of associated extent) are shown as a dotted line. The color version of this figure is available only in the electronic edition.

Holocene geomarkers of lake level (Reheis *et al.*, 2014). The study of such features has generated detailed Lahontan lake-level curves (Benson and Thompson, 1987; Adams *et al.*, 1999; Briggs *et al.*, 2005; Adams, 2012) that show the Sehoo highstand (~15.5 ka) to be abrupt, characterized by a rapid transgression that reached a maximum elevation of ~1337 m and followed by a rapid regression (Thompson *et al.*, 1986; Benson and Thompson, 1987; Adams and Wesnousky, 1998). Minor transgressions occurred during the late Pleistocene ($10{,}820 \pm 35$ ^{14}C yr B.P.) and the late Holocene (3595 ± 35 ^{14}C yr B.P.), reaching elevations of ~1230 and ~1199 m, respectively (Briggs and Wesnousky, 2005; Fig. 3). Previous mapping by Briggs and Wesnousky (2004) shows the distribution of late Pleistocene and Holocene shorelines and deposits along the northern section of the PLFZ (Fig. 3) and is utilized in this study to constrain the age of offset.

Table 1
Structure from Motion Modeling Parameters and Results

Site	Model Area (m^2)	Number of Images	Ground Control Points	Point Density (points/m^2)	Ground Resolution (m/pixel)	Root Mean Square (m)
1 and 2	189,278	971	43	130	0.04	0.07
3	101,181	326	11	238	0.06	0.09
4	78,432	88	18	1159	0.03	0.2
5	445,386	558	10	121	0.09	0.26
6	131,812	381	14	206	0.07	0.11
7	122,681	338	7	167	0.08	0.5

The trace of the PLFZ, from which we document seven offsets, lies almost entirely below the Lahontan Sehoo (~15.5 ka) highstand (Fig. 3). Further north, and closer to the modern shoreline, the trace of the fault is absent within the historic deposits of Pyramid Lake (Fig. 2). To constrain the age of offset, we assume the ages of offset lacustrine features, such as constructional shoreline features, are bound by the corresponding highstand above and below, such that lacustrine features between elevations 1337 and 1230 m have a maximum age of 15.5 ka and minimum age of 10.8 ka, and lacustrine deposits below 1230 m have a maximum age of 10.8 ka. Because of the brevity of the Sehoo highstand (15.5 ka) and rapid nature of the bounding transgression and following regression, we further assume that the age of offset deposits near the Sehoo highstand, whether they are transgressional or regressional in origin, to be very close in age to the highstand value of 15.5 ka. We therefore do not provide a minimum bound on deposits that sit within 15 m of the Sehoo highstand. Offset erosional geomorphic features, such as incised drainage channels, are assumed to form sometime after the occupation of the lake and are bound solely by the age of the Sehoo highstand (15.5 ka), providing a maximum age.

Methods

To produce high-resolution DEMs, we applied SFM to low-altitude aerial photography obtained from a low-flying remote-controlled multirotor UAV (a hobby "copter"). Because this is a relatively new technique, especially within the field of geomorphology and neotectonics, we first provide a general summary of SFM, followed by the methods we used.

Structure from Motion

Sprouting from stereophotogrammetry, SFM was developed during the late 1970s (Ullman, 1977, 1979) and rapidly progressed into simple automated workflows that, in combination with multiview stereo (MVS) (Pollefeys *et al.*, 2004), produce highly accurate 3D point data comparable with standard light detection and ranging (lidar) (Harwin and Lucieer, 2012; Westoby *et al.*, 2012). Recent applications of SFM include 3D modeling of iconic solitary structures (Snavely *et al.*, 2008), geologic outcrops (Westoby *et al.*, 2012), various geomorphic landscapes (Fonstad *et al.*, 2013; Johnson *et al.*, 2014), and paleoseismic trench exposures (Bemis *et al.*, 2014; Reitman *et al.*, 2015).

SFM uses photogrammetric triangulation of common features from a series of overlapping photographs from different and multiple perspectives in order to determine the camera position of each photograph, producing a camera model. MVS then uses the camera model to construct the 3D point model of the scene photographed, for which enhanced feature recognition algorithms allow for multiscaled photographs to have large changes in camera perspectives, allowing for detailed scene geometry (Pollefeys *et al.*, 2004). Feature color is also carried through the SFM/MVS process, providing red–green–blue values for each generated point. Recent applications and testing of SFM for topographic modeling show high levels of accuracies that are often comparable and sometimes better than standard lidar models (Harwin and Lucieer, 2012; Westoby *et al.*, 2012; Fonstad *et al.*, 2013; Johnson *et al.*, 2014). Unlike lidar, SFM does not have the potential to acquire ground points through dense vegetation canopies.

High-Resolution Topographic Models

We developed SFM topographic models of offset geomorphic features at seven individual sites along the trace of the PLFZ using aerial photographs obtained from a UAV. Sites were selected for the highest potential to record fault offset of geomorphic features. Low-altitude (< 30 m) aerial photographs were acquired at each site using a DJI Phantom 1 multirotor hobby copter mounted with a Ricoh GR 8.3 megapixel digital camera with a 5.9 mm lens. Photograph acquisition was focused along the trace of the fault, which allowed for the most image overlap and highest ground resolution along the fault (Table 1). During flight, images were captured every 5 s, producing ~100–950 photographs at each site, dependent on the size of the site (Table 1). Poor quality photographs, such as those that were blurred, contained obstructions, or were taken at very low altitude, were discarded from the modeling process.

Ground control points (GCPs) were deployed before photograph acquisition and incorporated in the modeling process to constrain scale. These consisted of 30-cm-diameter orange disks set up in rows of three, perpendicular to the fault and spaced ~50 m apart. The center of each GCP disk was geospatially located using a Trimble R10 RTK Global Positioning System, providing 2–5 cm accuracy.

We followed similar processing workflow procedures of Johnson *et al.* (2014) using AgiSoft PhotoScan Pro software. Dense point clouds of each site were produced in PhotoScan

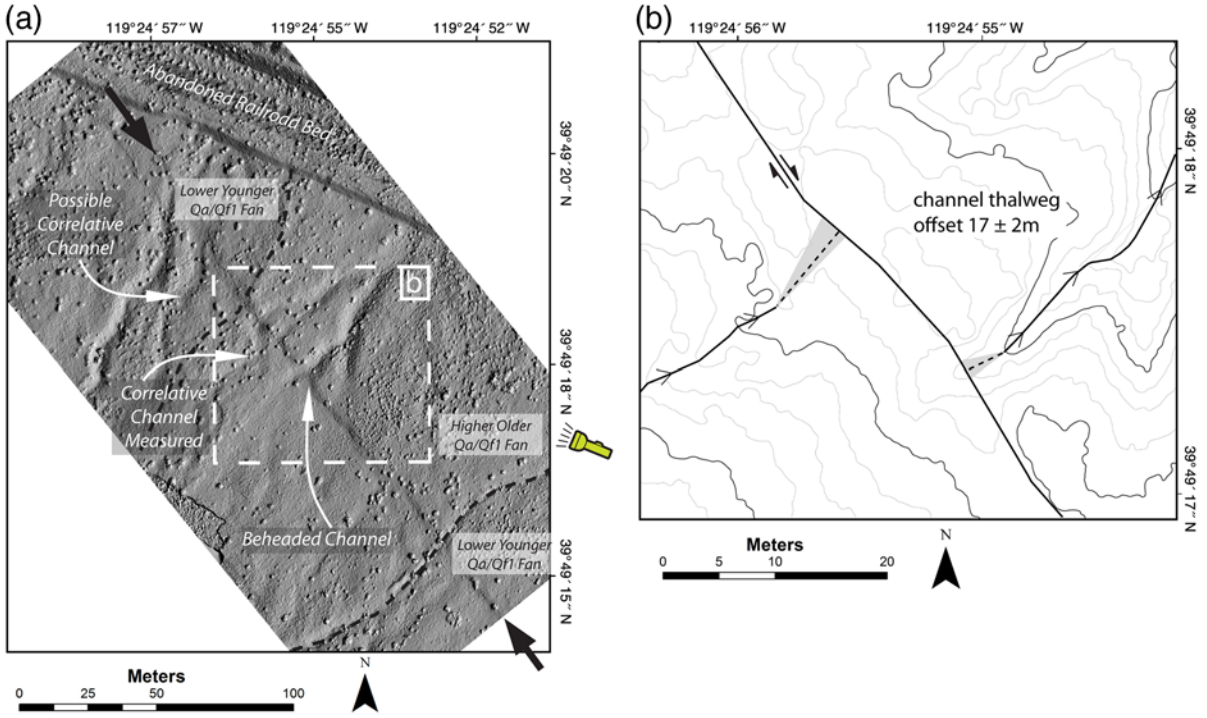

Figure 4. Site 1. (a) Hillshade map of fault trace and right-laterally displaced beheaded channel. (b) Contour map showing offset thalweg (solid and dotted thin black lines). The contour interval is 25 cm, with darker contours every 1 m. Uncertainty within the projection of the offset thalweg to the fault trace is indicated by the shaded areas. The color version of this figure is available only in the electronic edition.

using the suggested default settings. The DEMs were developed within PhotoScan using the dense point cloud and creating a Triangulated Irregular Network (also known as TIN). Suggested default settings were used in the TIN to maximize the face count, producing DEMs with 3–9 cm pixels (see Table 1). Our model accuracies, reported as root mean square values, range from 7 to 50 cm (Table 1). Hillshade, slope, and contour maps were produced in ArcGIS from the exported DEMs and further processed in ArcGIS for analysis and displacement estimates.

Vegetation filters were not used in our modeling process for the purpose of preserving the true landscape topography and because of the limited obstruction from local sagebrush. As a result, local sagebrush appears as irregular oval speckles within our hillshade models and causes irregular contour lines to be rough and irregular, sometimes only encircling a single sagebrush. To minimize these effects in our contour maps, we first applied a smoothing tool ("focal statistics" in ArcGIS) to our DEMs, which averages the value of each gridded cell over a defined area, 0.5–2 m in this case. We then removed contours encircling individual sagebrush using the contour line length as a filter, such that only long (> 15 m) continuous contour lines remain. Our hillshade images are not smoothed for the purpose of showing the landscape at the highest resolution.

Observations

We utilize our high-resolution hillshade, contour, and slope maps to define and estimate the amount of displacement and related uncertainties of linear geomorphic features (Figs. 4–10). Linear geomorphic features, such as ridge crests, shoreline scarp inflections, drainage thalwegs, and channel margins, serve as piercing points that are used to reconstruct fault displacement. At some sites, extrapolation of these linear features to the fault is required and often results in asymmetric uncertainties.

As described earlier, the age of offset is determined by the age of the surface on which the offset geomorphic deposit or feature is manifested (Fig. 3). The offset age is further used to estimate a slip rate by dividing the displacement estimates by the age of the offset features. We provide minimum and maximum slip rates in which the offset age is bound by Lahontan highstands; and, for those offset features not bound, such as incised drainage channels, we provide only a minimum rate.

Site 1

Site 1 is located in the northern end of the PLFZ, ~4 km south of the modern-day shoreline (Fig. 3). An uphill-facing fault scarp (Fig. 4a) cuts across a Qa/Qf1 fan that postdates the ~10,820 ± 35 B.P. late Pleistocene transgression of Lake Lahontan. The fan at this location is characterized by relatively higher older incised surfaces that sit within the interfluves of slightly lower younger surfaces (Fig. 4a). The lower, younger surfaces have a slightly smaller fault scarp and do not show offset within the incised drainages. Within a relatively older portion of the fan, a beheaded drainage channel is observed on the northeast side of the fault (Fig. 4).

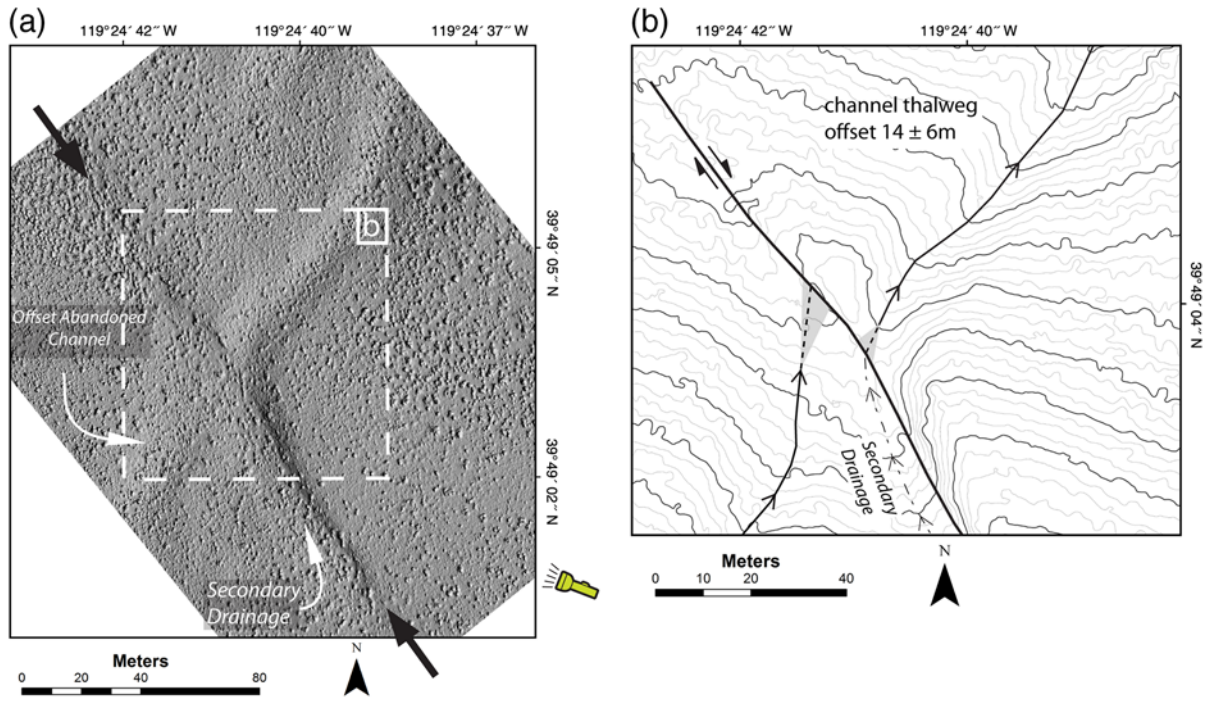

Figure 5. Site 2. (a) Hillshade map showing fault trace and right-laterally offset channel. (b) Contour map showing offset thalweg (black solid and dotted lines). The contour interval is 25 cm, with darker contours every 1 m. Uncertainty in projection of offset thalweg to trace indicated by shaded area. Uncertainty within the projection of the offset thalweg to the fault trace is indicated by shaded areas. The color version of this figure is available only in the electronic edition.

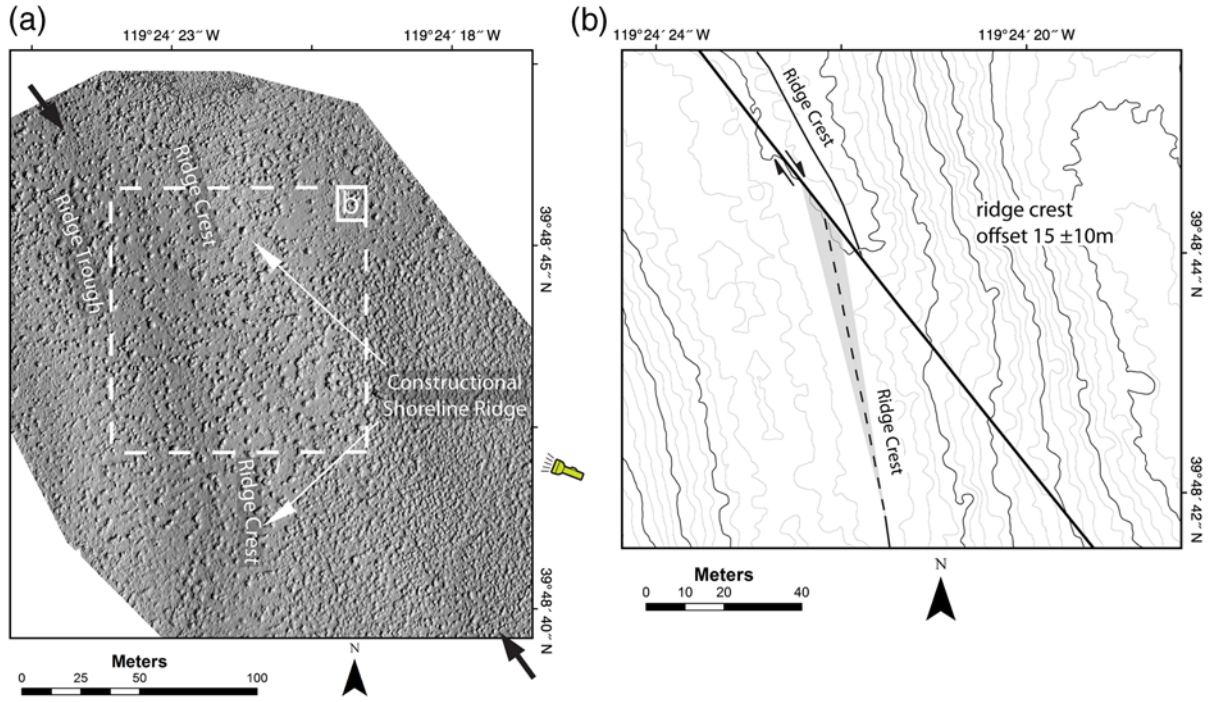

Figure 6. Site 3. (a) Hillshade map showing subtle fault trace and constructional shoreline feature. (b) Contour map showing offset ridge crest (black dashed line). The contour interval is 25 cm, with darker contours every 1 m. Uncertainty within the projection of the offset ridge crest to the fault trace is indicated by a shaded area. The color version of this figure is available only in the electronic edition.

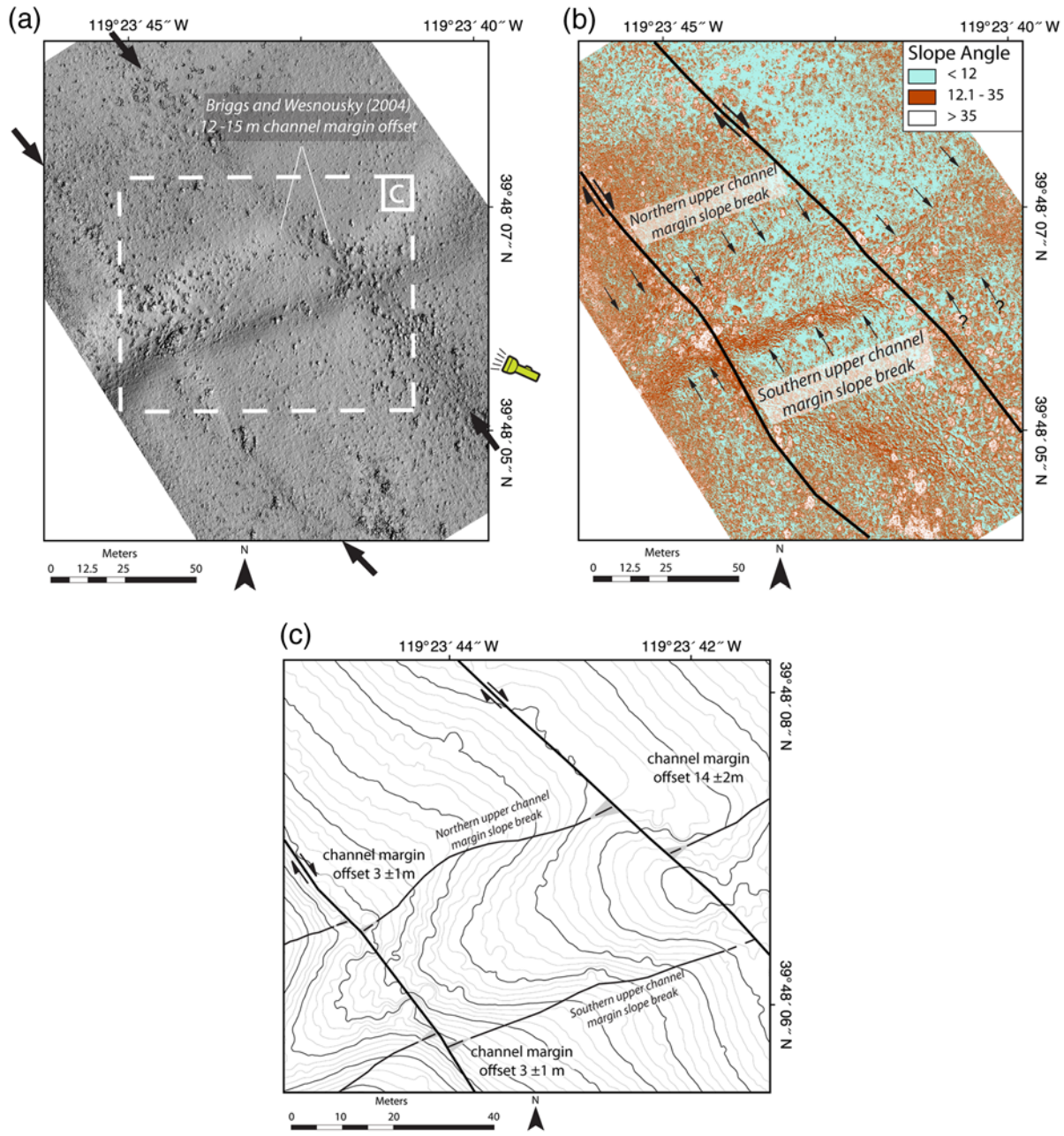

Figure 7. Site 4. (a) Hillshade map showing offset drainage and two strands of the PLFZ. (b) Slope map highlighting the top of channel margin walls (arrows), determined from a sharp break in slope. (c) Contour map showing offset channel margins (solid and dashed black lines) on each fault strand (solid black lines). Contour interval is 25 cm, with darker contours every 1 m. Uncertainty within the projection of the break in the slope that defines the channel margins to the fault strands is indicated by the shaded areas. The color version of this figure is available only in the electronic edition.

We interpret the thalweg of the correlative channel to be right-laterally offset by 17 ± 2 m on the southwest side of the fault (Fig. 4b). The qualitative uncertainty of the estimate reflects the poorly defined nature of the channel thalweg near the fault and on the southwest side of the fault (Fig. 4b). Assuming the displacement is tectonic and has accrued since the deposition of the alluvial fan unit (Qa/Qf1), the observations indicate a minimum slip rate of 1.6 ± 0.2 mm/yr.

We acknowledge another potential correlative channel on the southwest side of the fault, further north, that might be correlated to the beheaded channel (each labeled in Fig. 4a) and leads to an apparent right-lateral offset measurement of ~60 m. Because the correlative drainage sits within a relatively younger portion of the fan and the magnitude of this offset is very large, given the youthful age of the surface on which the offset is manifested (less than ~10.8 ka), we disregard the offset because it is unlikely tectonic. The offset would indicate a minimum slip rate of 5.5 mm/yr, well above prior findings (Briggs and Wesnousky, 2004) and others from this study and above the limits

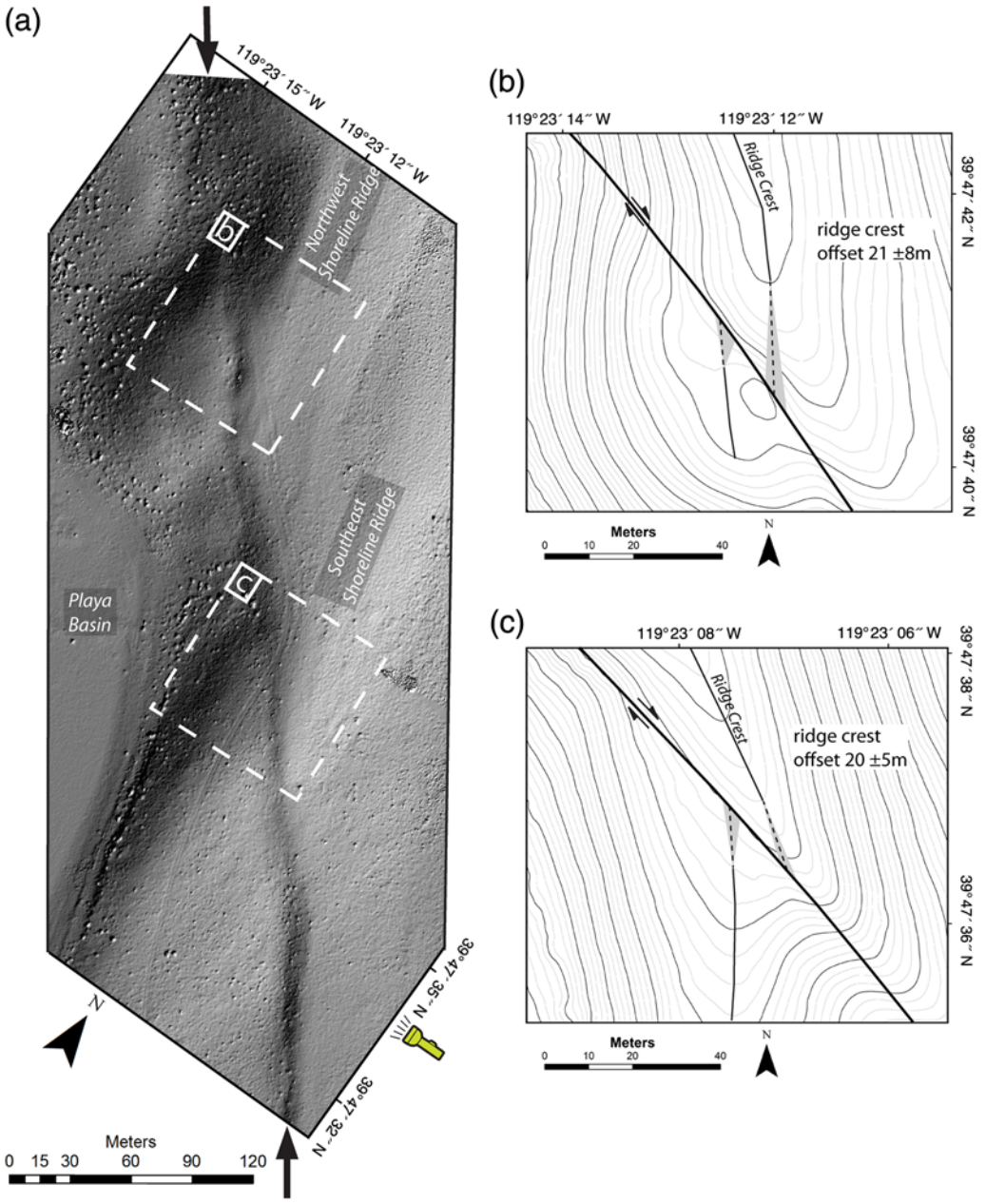

Figure 8. Site 5. (a) Hillshade map showing fault trace and offset shoreline features. (b) and (c) contour maps of (b) northwestern and (c) southeastern offset shoreline ridges. Solid and dotted black lines show the trace of ridge crests. The contour interval is 25 cm, with darker contours every 1 m. Uncertainty within the projection of the slope break to the fault trace is indicated by shaded areas. The color version of this figure is available only in the electronic edition.

placed by contemporary geodesy (Hammond *et al.*, 2011; Bormann, 2013).

Site 2

The fault at site 2 is expressed as a single linear uphill-facing scarp (up to ~1.5 m high) within Ql lacustrine deposits (Figs. 3 and 5). An abandoned channel intersects the fault at a high angle (Fig. 5a) and is right-laterally offset (Fig. 5b). The channel morphology is broad and muted, particularly on the southwest side of the fault, and introduces a moderate amount of uncertainty. Additionally, a secondary drainage, flowing north along the uphill-facing scarp, disrupts the morphology of the offset channel near the fault and adds to the uncertainty. We estimate 14 ± 6 m of right-lateral displacement of the thalweg across the fault (Fig. 5b). This channel incised into Ql lacustrine deposits sometime after the regression from the Sehoo highstand (~15.5 ka); the offset postdates ~15.5 ka and results in a minimum slip-rate estimate of 0.9 ± 0.4 mm/yr.

Site 3

Site 3 is located ~0.75 km southeast of site 2, where the fault is also expressed within Ql lacustrine deposits (Figs. 3

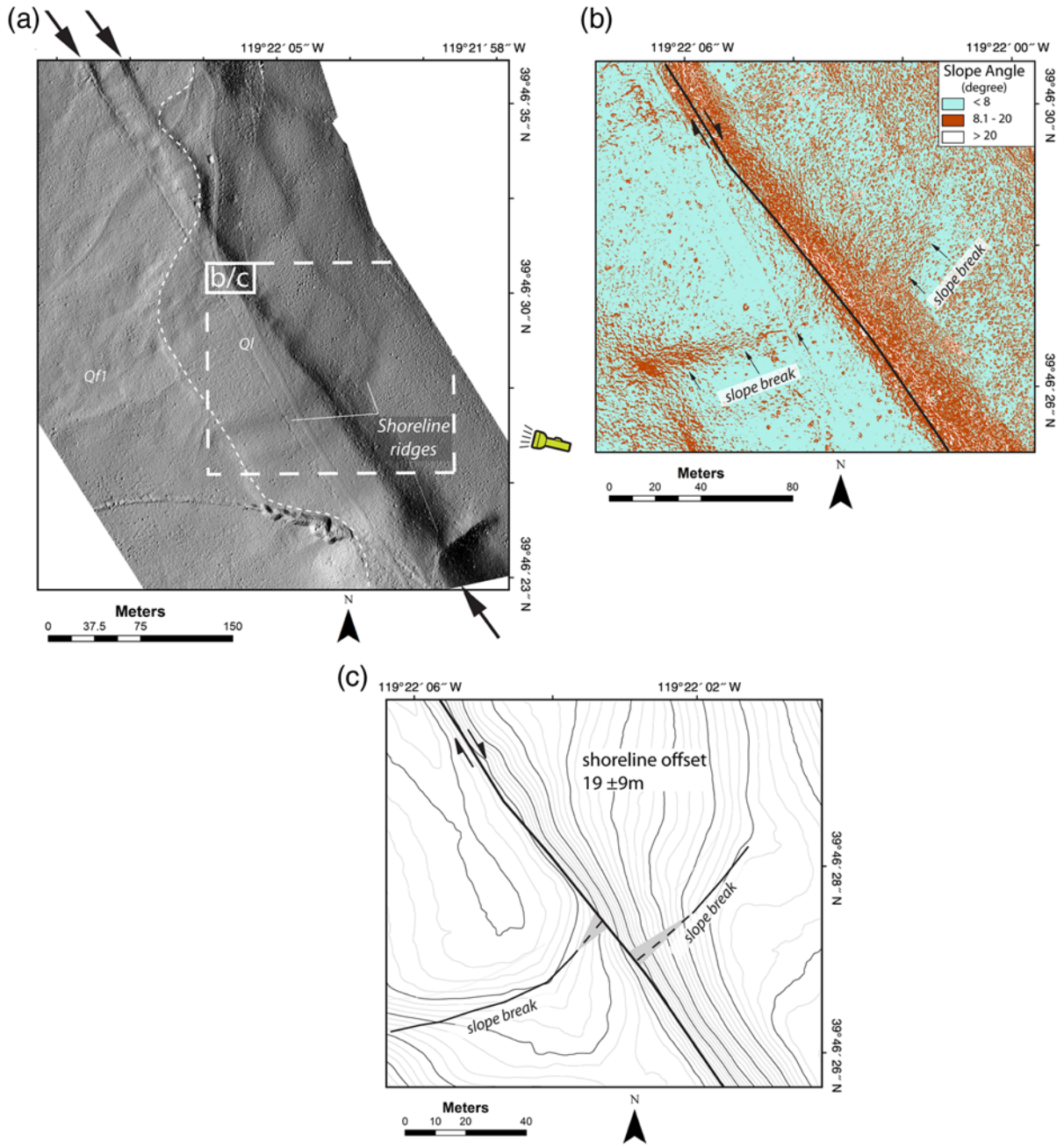

Figure 9. Site 6. (a) Hillshade map showing uphill-facing scarp and offset shoreline ridges. (b) Slope map defining slope break (arrows) on northwest face of the shoreline ridge. (c) Contour map showing the projection of the slope break into the fault (solid and dotted black lines). The contour interval is 25 cm, with darker contours every 1 m. Uncertainty within the projection of the slope break to the fault trace is indicated by shaded areas. The color version of this figure is available only in the electronic edition.

and 6). A broad constructional shoreline ridge intersects the trace of the Pyramid Lake fault at a highly oblique angle (Fig. 6a), and its crest is offset 15 ± 10 m (Fig. 6b). The broad nature of the ridge and its oblique intersection with the fault leads us to assign a relatively high uncertainty to the offset estimate. The offset Ql deposit here sits between the 15.5 ka Sehoo highstand and the 10.8 ka transgressional maximum, and so the offset measurement places a minimum bound on the fault-slip rate of about 1.0 ± 0.6 mm/yr and a maximum rate of 1.4 ± 0.9 mm/yr.

Site 4

The fault at site 4 is composed of two fault strands and forms a graben structure across Qf2 (Figs. 3 and 7). An abandoned drainage channel crosses both fault strands (Fig. 7a). The broad nature of the channel reduces our ability to constrain the thalweg using the contours (Fig. 7c). Instead, we use sharp slope breaks, determined on the generated slope map (Fig. 7b), of the upper channel margin walls as piercing points (small arrows in Fig. 7b). The northern channel wall is the most well defined and

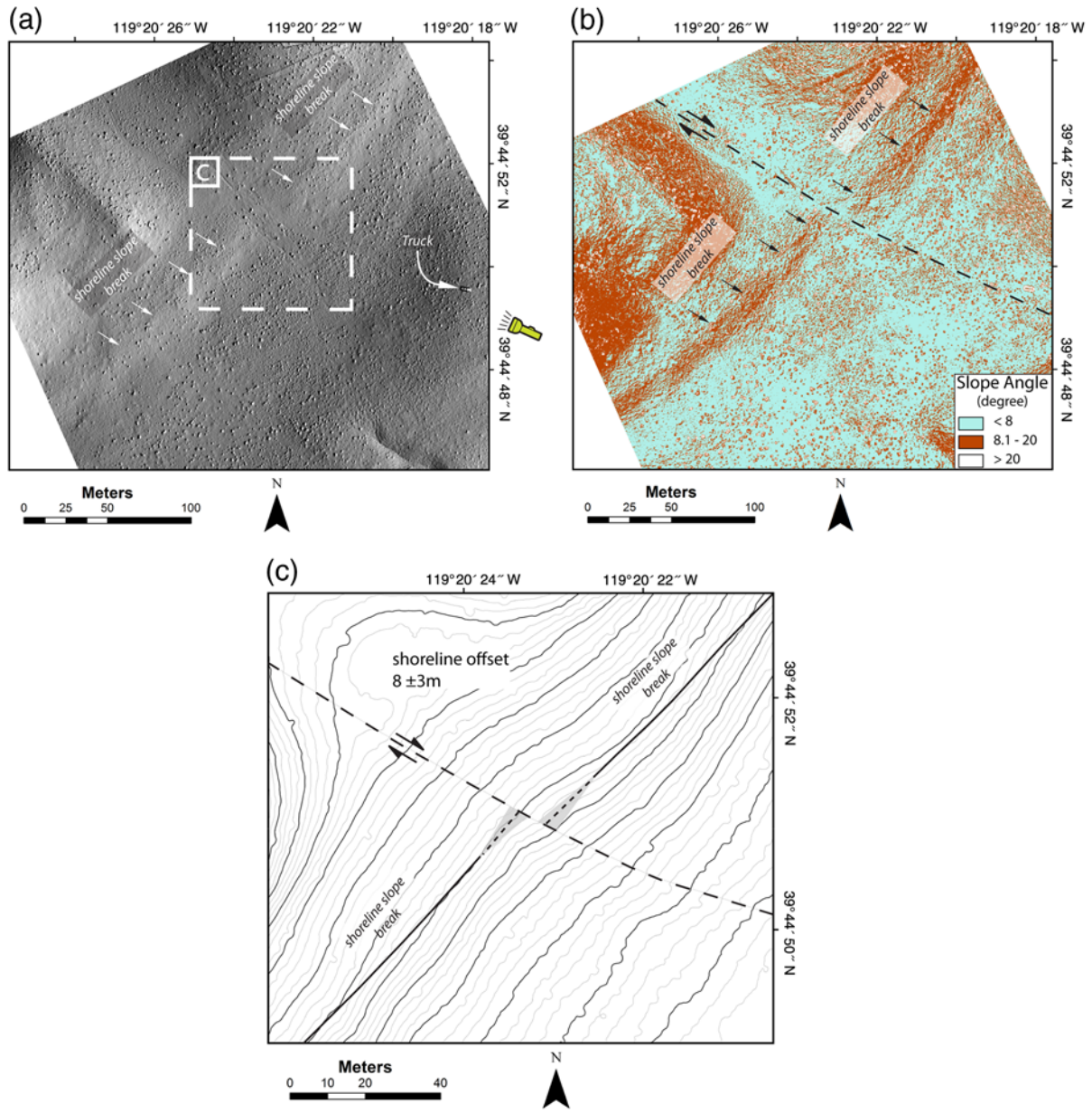

Figure 10. Site 7. (a) Hillshade map showing offset shoreline ridge. (b) Slope map defining slope break (arrows) on south face of the shoreline ridge. (c) Contour map showing displacement measurement of shorelines (traced with solid and dotted black lines). The contour interval is 25 cm, with darker contours every 1 m. Uncertainty within the projection of the slope break to the fault trace is indicated by shaded areas. The color version of this figure is available only in the electronic edition.

best records offset of the channel where it crosses the northeastern fault strand. We estimate 14 ± 2 m of right-lateral offset, similar to the offset estimate of 12–15 m at this site previously reported by Briggs and Wesnousky (2004). The sharpness of the slope break and its continuous nature to where it intersects the fault scarp allows us to assign a minimal uncertainty to the offset estimate. The southern margin of the channel is partly eroded and has a more muted slope break associated with the top of the southern channel margin wall. This is especially apparent east of the northeastern fault strand and does not provide a sufficient piercing point to measure.

Additional offset is recorded on the southwestern strand of the fault. The slope breaks at the top of both channel margin walls are well defined, particularly along the southern channel margin. We estimate that both the northern and the southern channel margins are similarly offset 3 ± 1 m. This offset was not observed by Briggs and Wesnousky (2004) and increases the total offset across the two fault strands to 17 ± 3 m. The accumulated offset of the drainage channel postdates the Lahontan highstand (15.5 ka) and yields a minimum slip-rate estimate of 1.1 ± 0.2 mm/yr.

Site 5

Site 5 is located at the southern end of a long (~1 km) linear northwest-trending wave-washed bedrock-cored ridge (Figs. 3 and 8a). The PLFZ intersects and displaces two broad but distinct shoreline ridges deposited on the bedrock-cored ridge (Fig. 8a). The crest of the northwestern ridge is right-laterally offset 21 ± 8 m (Fig. 8b), whereas the better-defined southeastern ridgeline is offset 20 ± 5 m (Fig. 8c). Using the age of the Sehoo highstand (15.5 ka) as a maximum bound on the age of the displaced shoreline ridges and using the larger measured offset (21 ± 8 m), we estimate a minimum fault-slip rate of 1.4 ± 0.5 mm/yr. This site also sits well above the 10.8 ka transgressional maximum, providing a minimum bound on the age of offset and a maximum slip-rate estimate of 1.9 ± 0.7 mm/yr.

Site 6

At site 6, arcuate constructional shoreline ridges that lie just below the Sehoo highstand (~1337 m) intersect the ~1-m-high uphill-facing fault scarp at a high angle (Figs. 3 and 9a). The break in slope on the northwest face of this shoreline ridge (Fig. 9b) is right-laterally offset 19 ± 9 m (Fig. 9c). The offset has accrued, at least, since the Lahontan highstand (15.5 ka), yielding a minimum slip-rate estimate of 1.2 ± 0.6 mm/yr. Because of the proximity (< 15 m) to the highstand, we assume this shoreline feature is very close in age to the Sehoo highstand (15.5 ka) and therefore do not provide a minimum age of offset.

Site 7

Site 7 is located at the southern end of a linear bedrock-cored ridge (Fig. 3). Here, shoreline escarpments that sit just below the Sehoo highstand wrap around the southern tip of the ridge (Figs. 3 and 10a). The fault trace is subtle and is better manifested by the offset of the shoreline (Fig. 10). The trend of the shoreline feature is best defined by the slope break at the top of the southeast-facing shoreline escarpment (Fig. 10b), which is offset 8 ± 3 m across the fault zone (Fig. 10c). The observed displacement has occurred since the formation of the shorelines, which must be very near to 15.5 ka in age because it lies just below the Sehoo highstand. We estimate a slip rate of 0.5 ± 0.2 mm/yr. Multiple fault traces exist at the latitude of this site (Figs. 2 and 3). Our slip-rate estimate here is for only one fault strand and is unlikely to have captured the entire near-field fault offset. Accordingly, the slip rate estimated here is relatively less than our other six sites.

Discussion and Conclusion

Our efforts provide a useful example of the application of small, low-cost UAV photography in neotectonic analysis. In this case, development of high-resolution DEMs resulted in the addition of seven measurable fault offsets along the PLFZ, more than doubling the previous amount of offset measurements from a prior study along the entire fault that used 1:10,000-scale low-sun-angle photography (Briggs and Wesnousky, 2004). In turn, these measurements provided us the ability to further evaluate the latest Pleistocene to Holocene slip rate of the PLFZ and its role in accommodating strain within the Walker Lane.

Reconciling Slip Rates on the Pyramid Lake Fault Zone

The offsets we observe at the seven sites range from 8 to 21 m, and yield slip rates range from 0.5 to 1.9 mm/yr (Fig. 11). The uncertainties we place on all are qualitative, in some cases quite large, and little weight might be given to any individual estimate. Together, minimum and maximum estimated slip rates from this study provide an average slip rate of 1.3 ± 0.4 mm/yr; and, among all of the slip rates determined along the entire PLFZ, including prior studies, all but two (site 7 in this study and site B of Briggs and Wesnousky, 2004) fall within this average slip rate (Fig. 11). Site 7 from this study was expected to be less because it is located where multiple fault traces exist and is likely not capturing all the slip. A principal observation, excluding site 7, is that our slip-rate estimates are broadly consistent among the six sites along the 17-km-long portion of the PLFZ that we studied and are invariably less than 2 mm/yr (Fig. 11). The values of our estimates are also less than the previously reported slip rate for the PLFZ, which was based on offset drainages at a single site along the Truckee River, about 7 km to the south of our most southern site (Figs. 2 and 11; Briggs and Wesnousky, 2004). There, drainages are interpreted to have incised into lacustrine deposits after the Sehoo highstand (post-15.5 ka), similar to most of the sites of offset reported in this study, and are reported to be offset 35–43 m. Such an offset yields a latest Pleistocene-to-Holocene slip rate of 2.6 ± 0.3 mm/yr, which is ~200–500% higher than the slip rates we document 7–20 km to the north.

Importantly, all of the measured offsets here and in Briggs and Wesnousky (2004) provide a minimum slip rate. This means that slip-rate calculations, other than at site 1, assume that the age of the Sehoo highstand (15.5 ka) marks the time at which offset features begin recording displacement. Some disparity in rates might arise because some of the offset drainages did not develop immediately upon desiccation of the lake. Yet, several of the sites we measured (sites 6 and 7) are shoreline depositional features, which developed very closely in time to the Sehoo highstand and would be expected to record all of the displacement since the highstand. Additionally, our largest measurement of offset (site 5) is also of displaced lacustrine depositional features that postdates the Sehoo highstand and predates the late Pleistocene transgression (10.8 ka). It is unlikely that the observed variation in slip rate along fault strike from our measurements has not captured the majority of slip since the highstand.

Our estimates of offset and slip rate are located along the northern section of the PLFZ, whereas the higher slip rate re-

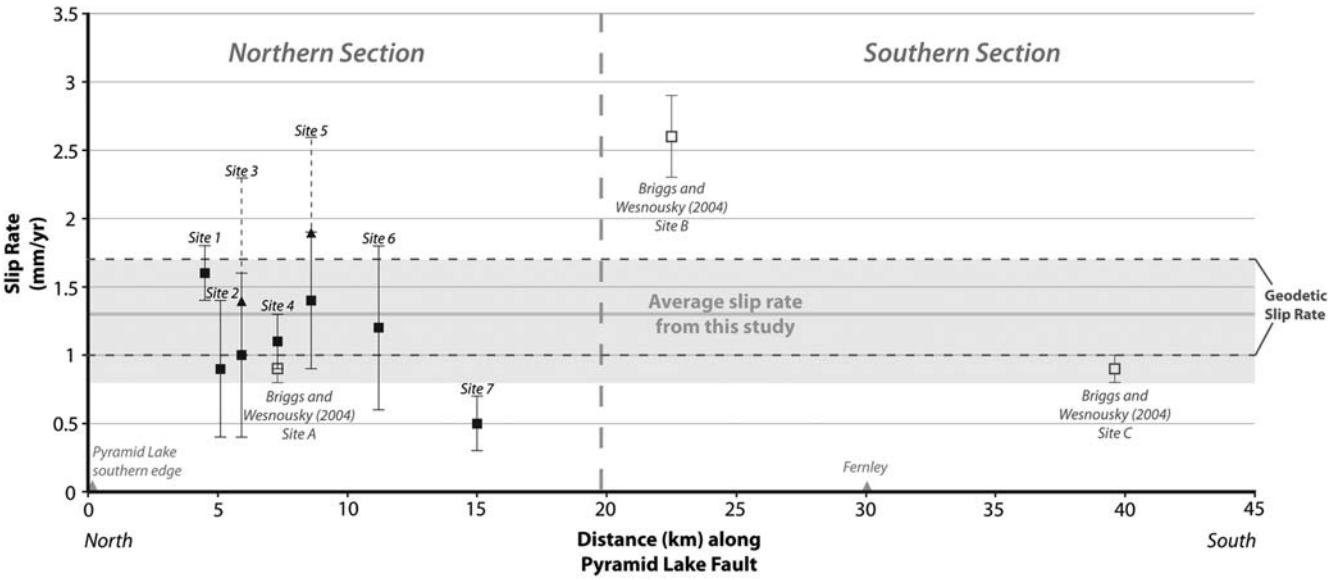

Figure 11. Summary of slip-rate estimates along the PLFZ. The solid black boxes are minimum slip rates obtained from this study, with associated uncertainties shown by extending solid gray lines. Black triangles show the maximum slip rates obtained in this study, and associated uncertainty is shown as the extending dotted lines. The gray shaded region and the horizontal thick solid gray line display the average slip-rate range obtained from this study. Slip rates and associated uncertainties from Briggs and Wesnousky (2004) are shown as open dark gray boxes. The horizontal dashed lines bound the limit of slip rates estimated for the PLFZ from block modeling of contemporary geodetic data (Hammond *et al.*, 2011; Bormann, 2013). The thick vertical dashed line shows the approximate location between the northern section and southern section of the PLFZ.

ported by Briggs and Wesnousky (2004) was determined along the southern section of the fault (Figs. 2 and 11). The two sections of the fault are separated by the junction of the conjugate left-lateral Olinghouse fault (Fig. 2), which forms a kinematically and structurally complex zone near the intersection. It might be suggested that the southern section of the fault is, indeed, slipping faster than the northern section because slip from the southern section is being transferred in part to the Olinghouse fault. This would kinematically require a component of reverse slip on the Olinghouse fault. However, the trace of the Olinghouse fault exhibits extensional features near its intersection with the PLFZ (Bell *et al.*, 2005; Briggs and Wesnousky, 2005), and thus this idea does not support the disparate slip rates for the southern and northern fault sections.

It could also be suggested that the large offset of Briggs and Wesnousky (2004) is the result of the central location of the offset site along the entire fault, where the highest amounts of slip are to be expected (e.g., Bürgmann *et al.*, 1994; Jónsson *et al.*, 2002). Our observations do not refute this idea because they are all located to the north and are of lesser value. The large offset of Briggs and Wesnousky (2004) is located only 7 km south of our smallest measured offset (8 ± 3 m) and would suggest a significant decay in slip amount within a short distance.

Two observations support the notion that a lesser value of slip rate than the previously reported 2.6 mm/yr is a better representation of the Pyramid Lake fault-slip rate. First, the range of the best-estimated slip rates (0.5–1.6 mm/yr) reported in this article is consistent with recent geodetically estimated slip rates for the Pyramid Lake fault, which range from 1.0 to 1.7 mm/yr (Fig. 11; Hammond *et al.*, 2011; Bormann, 2013). Second, the displacements measured in this study yield greater consistency with the paleoearthquake history of displacement that has been reported along the fault.

Previous paleoseismic trenching along the northern section of the Pyramid Lake fault has shown evidence for at least four, possibly five, seismic events since the 15.5 ka Lahontan Sehoo highstand (Anderson and Hawkins, 1984; Briggs and Wesnousky, 2004). The latest three are determined to have occurred after 8980 ± 260 yr B.P., constraining the reoccurrence interval to ~2910–3080 yr (Briggs and Wesnousky, 2004). Together, these observations suggest that the higher number of earthquakes (five) satisfies the reoccurrence interval. If these five events are responsible for the latest Pleistocene displacement along the fault, the 35–42 m of offset reported in Briggs and Wesnousky (2004) requires that individual coseismic displacements have averaged 7–9 m, which is significantly larger than would generally be expected from empirical scaling relationships for a strike-slip fault of its 45 km length (Wells and Coppersmith, 1994; Wesnousky, 2008). The range of offsets reported here is significantly less, ranging from 14 to 21 m. These offsets require that coseismic offsets average only between 3–5 m, more in line with the magnitude of displacements predicted by regressional relations derived from historical earthquakes (e.g., Wells and Coppersmith, 1994; Wesnousky, 2008).

The absence of a paleoearthquake record on the southern section of the PLFZ allows for the possibility of the southern section to rupture independently and possibly contain more events, which would allow for the higher amount of observed slip. This would require many more events on the southern section than the northern, and expression of this is lacking within the geomorphology along the southern section of the fault.

In the end, our observations do not directly disprove the higher slip rate reported in Briggs and Wesnousky (2004). However, they do permit the suggestion that the part of the offset on which their high-slip-rate estimate was based may record some component of stream deflection as well as offset and thus overestimates the true offset along the fault.

Implications to Northern Walker Lane Kinematics

Mismatch between geodetic strain rates and geologic slip rates persist within the Walker Lane. This issue has been exemplified in the northern Walker Lane (Wesnousky *et al.*, 2012; Gold *et al.*, 2013), where the total geologic slip rate of 1.4–3.3 mm/yr summed across the Mohawk Valley fault, Grizzly Valley fault, Honey Lake fault, and the Warm Springs fault (Fig. 1), fails to match the most recent geodetically determined rate of ~5 mm/yr (Hammond *et al.*, 2011; Bormann, 2013).

This mismatch also exists further south (Wesnousky *et al.*, 2012), at the latitude of the PLFZ, and is exacerbated by the new slower rates presented in this study (Fig. 11). Here, recent geodetic rates estimate ~7 mm/yr of contemporary strain (Fig. 1; Bormann, 2013). Summing the geologically determined slip rates of known active right-lateral strike-slip faults across this transect, which only includes 0.3–0.4 mm/yr on the Polaris fault (Hunter *et al.*, 2011) and the <2 mm/yr rate on the PLFZ from this study, yields a maximum slip rate of ~2.4 mm/yr. This yields a minimum deficit of ~4.2 mm/yr. It may be inferred from the deficit that (1) there is unidentified oblique slip on mapped normal faults; (2) there are unidentified active strike-slip faults within the geodetic transect; (3) strike-slip motion is being accommodated by some other means, such as block rotation (Wesnousky *et al.*, 2012); (4) significant off-fault deformation occurs coseismically and cannot be observed by paleoseismology or near-field neotectonic studies, such as this (Gold *et al.*, 2015); or (5) unknown combinations of these possible explanations contribute to this deficit.

Implications to Seismic Hazard

If one accepts that the relatively lesser geologic slip rate we find for the PLFZ, as compared with prior estimates from geology, is correct, the consequence to seismic hazard in the nearby Reno area is twofold and in some sense counteracting. Prior earthquake studies provide the best measures of the expected repeat time of earthquakes along the PLFZ, and the reduction in slip rate reduces the magnitude of coseismic slip in repeating earthquakes needed to explain the slip rate. This, in effect, reduces the seismic hazard imposed by the fault on the Reno area. When coupling the observation of reduced slip rate with current geodetic observations that indicate shear equivalent to 7 mm/yr is accruing at this latitude of the Walker Lane (Bormann, 2013) and that the PLFZ marks the eastern margin of the Walker Lane, the slip once attributed to the PLFZ must ultimately be accounted for by slip and thus by earthquakes on a fault or faults further west, perhaps closer to Reno, which would increase the level of seismic hazard for Reno. The finding of a lower slip rate on the PLFZ thus exacerbates prior observations in the northern section of the Walker Lane that geologic rates of slip are insufficient to account for the slip budget indicated by contemporary geodesy (Wesnousky *et al.*, 2012; Gold *et al.*, 2013).

Data and Resources

Base-map data for Figures 1 and 2 were acquired from the National Elevation Dataset (http://ned.usgs.gov/about.html, last accessed August 2014). Quaternary active fault traces in Figure 1 were acquired from the U.S. Geological Survey Quaternary Fault and Fold database (http://earthquake.usgs.gov/hazards/qfaults, last accessed October 2015). All other data in this article were self-collected in January–August 2014 and have not been previously published.

Acknowledgments

This research was supported in part by U.S. Geology Survey (USGS) National Earthquake Hazards Reduction Program Grant Number G13AP00033. We are truly grateful toward the Pyramid Lake Paiute Tribe for granting us permission to conduct this study on tribal lands. In particular, we thank Beverly Harry for her participation and guidance throughout the duration of our fieldwork. We also thank several University of Nevada, Reno graduate students; Kyle Basler-Reeder, Greg Dering, Ian Pierce, and Courtney Brailo, who assisted in the collection of data in the field. Reviews from Scott Bennett, Michael Bund, and Associate Editor Brian Sherrod significantly improved the quality and clarity of this article, and we are appreciative of their insightful comments and suggestions. Any use of trade, firm, or product names is for descriptive purposes only and does not imply endorsement. This is Center of Neotectonics Contribution Number 66.

References

Adams, K. D. (2012). Response of the Truckee River to lowering base level at Pyramid Lake, Nevada, based on historical air photos and lidar data, *Geosphere* **8,** no. 3, 607–627.

Adams, K. D., and S. G. Wesnousky (1998). Shoreline processes and the age of the Lake Lahontan highstand in the Jessup embayment, Nevada, *Geol. Soc. Am. Bull.* **110,** no. 10, 1318–1332.

Adams, K. D., S. G. Wesnousky, and B. G. Bills (1999). Isostatic rebound, active faulting, and potential geomorphic effects in the Lake Lahontan basin, Nevada and California, *Geol. Soc. Am. Bull.* **111,** no. 12, 1739–1756.

Anderson, L. W., and F. F. Hawkins (1984). Recurrent Holocene strike-slip faulting, Pyramid Lake fault zone, western Nevada, *Geology* **12,** no. 11, 681–684.

Arrowsmith, J. R., and O. Zielke (2009). Tectonic geomorphology of the San Andreas fault zone from high resolution topography: An example from the Cholame segment, *Geomorphology* **113,** nos. 1/2, 70–81.

Bell, E. J., and D. B. Slemmons (1979). Recent crustal movements in the central Sierra Nevada Walker Lane region of California–Nevada. 2. Pyramid Lake right-slip fault zone segment of the Walker Lane, *Tectonophysics* **52,** nos. 1/4, 571–583.

Bell, J. W., K. House, and R. Briggs (2005). *Geologic Map of the Nixon Area, Washoe County, Nevada*, Nevada Bureau of Mines and Geology, scale 1:24,000.

Bemis, S. P., S. Micklethwaite, D. Turner, M. R. James, S. Akciz, S. T. Thiele, and H. A. Bangash (2014). Ground-based and UAV-based photogrammetry: A multi-scale, high-resolution mapping tool for structural geology and paleoseismology, *J. Struct. Geol.* **69,** 163–178.

Benson, L. V., and R. S. Thompson (1987). Lake-level variation in the Lahontan basin for the past 50,000 years, *Quaternary Res.* **28,** no. 1, 69–85.

Bormann, J. M. (2013). New insights into strain accumulation and release in the central and northern Walker Lane, Pacific-North American plate poundary, California and Nevada, USA, *Ph.D. Dissertation*, University of Nevada, Reno, 150 pp.

Briggs, R. W., and S. G. Wesnousky (2004). Late Pleistocene fault slip rate, earthquake recurrence, and recency of slip along the Pyramid Lake fault zone, northern Walker Lane, United States, *J. Geophys. Res.* **109,** no. B8, 16.

Briggs, R. W., and S. G. Wesnousky (2005). Late Pleistocene and Holocene paleoearthquake activity of the Olinghouse fault zone, Nevada, *Bull. Seismol. Soc. Am.* **95,** no. 4, 1301–1313.

Briggs, R. W., S. G. Wesnousky, and K. D. Adams (2005) Late Pleistocene and late Holocene lake highstands in the Pyramid Lake Sub-basin of Lake Lahontan, Nevada, USA, *Quaternary Res.* **64,** no. 2, 257–263.

Bürgmann, R., D. D. Pollard, and S. J. Martel (1994). Slip distributions on faults: Effects of stress gradients, inelastic deformation, heterogeneous host-rock stiffness, and fault interaction, *J. Struct. Geol.* **16,** no. 12, 1675–1690.

Eisses, A. K., A. Kell, G. M. Kent, N. W. Driscoll, R. L. Baskin, K. D. Smith, R. E. Karlin, J. N. Louie, and S. K. Pullammanappallil (2015) New constraints on fault architecture, slip rates, and strain partitioning beneath Pyramid Lake, Nevada, *Geosphere* **11,** no. 3, 683–704.

Fonstad, M. A., J. T. Dietrich, B. C. Courville, J. L. Jensen, and P. E. Carbonneau (2013). Topographic structure from motion: A new development in photogrammetric measurement, *Earth Surf. Processes Landforms* **38,** no. 4, 421–430.

Gold, R. D., N. G. Reitman, R. W. Briggs, W. D. Barnhart, G. P. Hayes, and E. Wilson (2015). On- and off-fault deformation associated with September 2013 M_w 7.7 Balochistan earthquake: Implications for geologic slip rate measurements, *Tectonophysics* **660,** 65–78.

Gold, R. D., W. J. Stephenson, J. K. Odum, R. W. Briggs, A. J. Crone, and S. J. Angster (2013). Concealed Quaternary strike-slip fault resolved with airborne lidar and seismic reflection: The Grizzly Valley fault system, northern Walker Lane, California, *J. Geophys. Res.* **118,** no. 7, 3753–3766.

Hammond, W. C., G. Blewitt, and C. Kreemer (2011). Block modeling of crustal deformation of the northern Walker Lane and basin and range from GPS velocities, *J. Geophys. Res.* **116,** 28.

Harwin, S., and A. Lucieer (2012). Assessing the accuracy of georeferenced point clouds produced via multi-view stereopsis from unmanned aerial vehicle (UAV) imagery, *Rem. Sens.* **4,** no. 6, 1573–1599.

Hunter, L. E., J. F. Howle, R. S. Rose, and G. W. Bawden (2011). Lidar-assisted identification of an active fault near Truckee, California, *Bull. Seismol. Soc. Am.* **101,** no. 3, 1162–1181.

Johnson, K., E. Nissen, S. Saripalli, J. R. Arrowsmith, P. McGarey, K. Scharer, P. Williams, and K. Blisniuk (2014). Rapid mapping of ultrafine fault zone topography with structure from motion, *Geosphere* **10,** no. 5, 969–986.

Jónsson, S., H. Zebker, P. Segall, and F. Amelung (2002). Fault slip distribution of the 1999 M_w 7.1 Hector Mine, California, earthquake, estimated from satellite radar and GPS measurements, *Bull. Seismol. Soc. Am.* **92,** no. 4, 1377–1389.

Pollefeys, M., L. V. Gool, M. Vergauwen, F. Verbiest, K. Cornelis, J. Tops, and R. Koch (2004). Visual modeling with a hand-held camera, *Int. J. Comput. Vis.* **59,** no. 3, 207–232.

Reheis, M. C., K. D. Adams, C. G. Oviatt, and S. N. Bacon (2014). Pluvial lakes in the Great Basin of the western United States—A view from the outcrop, *Quaternary Sci. Rev.* **97,** 33–57.

Reitman, N. G., S. E. Bennett, R. D. Gold, R. W. Briggs, and C. B. DuRoss (2015). High-resolution trench photomosaics from image-based modeling: Workflow and error analysis, *Bull. Seismol. Soc. Am.* **105,** no. 5, 2354–2366.

Sanders, C. O., and D. B. Slemmons (1996). Geomorphic evidence for Holocene earthquakes in the Olinghouse fault zone, Western Nevada, *Bull. Seismol. Soc. Am.* **86,** no. 6, 1784–1792.

Snavely, N., S. M. Seitz, and R. Szeliski (2008). Modeling the world from Internet photo collections, *Int. J. Comput. Vis.* **80,** no. 2, 189–210.

Thompson, R. S., L. V. Benson, and E. M. Hattori (1986). A revised chronology for the last Pleistocene lake cycle in the central Lahontan basin, *Quaternary Res.* **25,** 1–9.

Ullman, S. (1977). Structure from motion, *J. Opt. Soc. Am.* **67,** no. 10, 1400–1400.

Ullman, S. (1979). The interpretation of structure from motion, *Proc. Roy. Soc. Lond. B Biol. Sci.* **203,** no. 1153, 405–426.

Wells, D. L., and K. J. Coppersmith (1994). New empirical relationships among magnitude, rupture length, rupture width, rupture area, and surface displacement, *Bull. Seismol. Soc. Am.* **84,** no. 4, 974–1002.

Wesnousky, S. G. (2008). Displacement and geometrical characteristics of earthquake surface ruptures: Issues and implications for seismic-hazard analysis and the process of earthquake rupture, *Bull. Seismol. Soc. Am.* **98,** no. 4, 1609–1632.

Wesnousky, S. G., J. M. Bormann, C. Kreemer, W. C. Hammond, and J. N. Brune (2012). Neotectonics, geodesy, and seismic hazard in the northern Walker Lane of western North America: Thirty kilometers of crustal shear and no strike-slip? *Earth Planet. Sci. Lett.* **329,** 133–140.

Westoby, M. J., J. Brasington, N. F. Glasser, M. J. Hambrey, and J. M. Reynolds (2012). "Structure-from-motion" photogrammetry: A low-cost, effective tool for geoscience applications, *Geomorphology* **179,** 300–314.

Zielke, O., Y. Klinger, and J. R. Arrowsmith (2015). Fault slip and earthquake recurrence along strike-slip faults—Contributions of high-resolution geomorphic data, *Tectonophysics* **638,** 43–62.

Center for Neotectonics Studies
University of Nevada
MS169 1664 North Virginia Street
Reno, Nevada 89557
sangster@nevada.unr.edu
wesnousky@unr.edu
(S.A., S.W.)

Institute of Geology
China Earthquake Administration
Building No. 1, Yard No. 1 jia, Hua Yan Li
Chaoyang District, Beijing, China
huangweiliang1987@gmail.com
(W.H.)

Nevada Seismological Laboratory
University of Nevada
MS 174
1664 North Virginia Street
Reno, Nevada 89557
gkent@unr.edu
(G.K.)

Department of Geography
Hiroshima University
1-3-1 Kagamiyama
Higashihiroshima 739-8526, Japan
tnakata@hiroshima-u.ac.jp
(T.N.)

Department of Geography
Hiroshima University
1-5-1 Kagamiyama
Higashihiroshima 739-8526, Japan
hgoto@hiroshima-u.ac.jp
(H.G.)

Manuscript received 20 November 2015;
Published Online 2 February 2016